Multiscale Investigations of Drift-Wave Turbulence and Plasma Flows: Measurements and Total-Distribution-Function Gyrokinetic Simulations

S. Leerink,[1] V. V. Bulanin,[2] A. D. Gurchenko,[3] E. Z. Gusakov,[3] J. A. Heikkinen,[4] S. J. Janhunen,[1] S. I. Lashkul,[3] A. B. Altukhov,[3] L. A. Esipov,[3] M. Yu. Kantor,[3] T. P. Kiviniemi,[1] T. Korpilo,[1] D. V. Kuprienko,[2] and A. V. Petrov[2]

[1]*Euratom-Tekes Association, Aalto University, P.O. Box 4100, FI-02015 Aalto, Finland*
[2]*St. Petersburg State Polytechnical University, St. Petersburg, Russia*
[3]*Ioffe Physical-Technical Institute of the RAS, St. Petersburg, Russia*
[4]*Euratom-Tekes Association, VTT, P.O. Box 1000, FI-02044 VTT, Finland*

(Received 13 April 2012; published 17 October 2012)

Direct measurements of micro-, meso-, and macroscale transport phenomena in the FT-2 tokamak are shown to be quantitatively reproduced by global full f nonlinear gyrokinetic simulation predictions. A detailed agreement with mean equilibrium $E \times B$ flows, oscillating fine-scale zonal flows, and turbulence spectra observed by a set of sophisticated microwave backscattering techniques as well as a good fit of the thermal diffusivity data are demonstrated. A clear influence of the impurity ions on the fluctuating radial electric field is observed.

DOI: 10.1103/PhysRevLett.109.165001 PACS numbers: 52.25.Fi, 52.35.Ra, 52.65.Tt, 52.70.Gw

The complex interaction between large-scale mean $E \times B$ flows, fine-scale zonal flows, and turbulence is of importance for transport of energy and particles in magnetically confined plasmas [1,2]. Massively parallelized gyrokinetic total distribution simulations of the coupled Boltzmann-Maxwell system of equations allow for first principles based studies of this interplay, as the processes above are all in one simulation. In this Letter, for the first time, global gyrokinetic particle-in-cell simulations will be quantitatively compared to experimentally observed mean equilibrium $E \times B$ flows, fine-scale zonal flows, and oscillations of such flows in the presence of tokamak plasma drift-wave turbulence. Both the shift and the broadening of the turbulence frequency spectra of synthetic and experimental Doppler reflectometry (DR) diagnostics, as well as the probability distribution function, the standard deviation, and the dominant frequency of the simulated and experimental radial electric field fluctuations will be investigated.

The small FT-2 tokamak low current Ohmic L-mode conditions are adopted as a basis (major radius $R_0 =$ 55 cm, minor radius $a = 8$ cm, $\rho^* = v_s/(\Omega_i a) = 0.003-$ 0.02 with Ω_i the ion gyrofrequency and v_s the sound velocity, total plasma current $I = 18.9$ kA, radial current density dependence $j(r) = j_0[1 - (r/a)^2]^3$, on-axis magnetic field $B_0 = 2.3$ T, effective collisionality $\nu^* = 10$–25, $Z_{\text{eff}} = 3.1$, and oxygen 6^+ as a main impurity at initialization density $N_I = 0.07 \times N_e$ as determined by using visible light spectroscopy and loop voltage measurements). With $\beta \ll 1$, typical for the FT-2 tokamak, the electrostatic assumption with a fixed magnetic field background is legitimized. The plasma is bounded by a pair of poloidal limiters allowing a simpler simulation than a divertor tokamak. The plasma energy confinement time is about 1 ms which is 2–3 orders of magnitude higher than the linear growth time and the decorrelation time of the main underlying trapped electron instability. The main plasma energy losses are by heat conduction or convection and impurity radiation and ionization, whereas the heat source is by Ohmic heating only.

The simulations are done with the global electrostatic particle-in-cell code ELMFIRE [3] to find the total distribution function (full f) of drift kinetic electrons and any selection of gyrokinetic plasma ions. A simulation region of $\rho = r/a = [0.25 - 1]$ and a time step of $\Delta t = 30$ ns are employed. The spatial grid is set to $120 \times 150 \times 8$ in the radial (r), poloidal (θ), or toroidal (ϕ) direction which limits the narrowest resolvable density fluctuations to the order of the ion Larmor radius. Neumann and Dirichlet boundary conditions for the potential are used at the inner and outer boundary, respectively. Collisions are modeled by a momentum and energy conserving binary collision model between all particle species [4], and a toroidal angular momentum conserving interpolation scheme for the electric field is applied [5]. The particles are initialized according to a prescribed temperature and density profile and are allowed to self-consistently develop in time while turbulence develops and heat sources and sinks are applied. Electrons are cooled according to the fit of the power density of the impurity radiation and ionization distribution provided by vertically scanned bolometric measurements resulting in dependence $P_{\text{rad}} = 3.5 \times 10^6(-0.16\rho e^{(8\rho-8)} + 0.08\rho + 0.15)$ W/m^3. Ohmic heating is inherent by a feedback in the radially uniform loop voltage ramping up and sustaining the total plasma current, obtaining a 2.25 V loop voltage for the steady state solution.

Particles passing the inner boundary are reflected back into the simulation domain, whereas particles passing the outer boundary are reinitialized into the simulation domain

as an electron-ion pair according to a prescribed profile based on deduction from the measured radial profile of the neutral hydrogen density. This particle outflow caused by the two poloidal limiters is modeled by assigning a random toroidal distance, ranging between 0 and πR_0, to each ion entering the outer layer of the simulation domain. When the ion has traveled this distance, it is reinitialized back into the plasma. For every removed ion, a random electron from the same radial position is simultaneously removed. This model successfully prevents particle accumulation near the outer boundary and captures the most prominent features of the recycling process. The simulations were performed in two parts, where the first 180 μs were performed by removing modes with toroidal mode number $n \neq 0$ to obtain the neoclassical equilibrium, after which the filtering was switched off and turbulence was allowed to develop for another 180 μs. On average, each cell contained 3000 particles of each species obtaining a random noise level lower than 1% at which convergence of the fluxes was achieved [6].

The initial electron density and temperature profiles were provided by Thomson scattering, and the ion temperature was measured by the charge-exchange diagnostic for $r < 4$ cm and visible light spectroscopy for $r > 5$ cm. The initial impurity and hydrogen temperatures were assumed to be equal. Figure 1 presents the experimental profiles, including the uncertainty estimations, and the simulated input and steady state profiles for the turbulent stage of the simulation. The electron and main ion heat conductivity $\chi_j = q_j/(n_j \nabla_r T_j)$, with q_j the heat flux, are obtained from the experimental profiles using ASTRA modeling [7] for the former one and energy balance in the ion channel for the latter one and compared to the ELMFIRE predictions of the energy flux Q_j and particle flux Γ_j with the relation $q_j = Q_j - \frac{3}{2} T_j \Gamma_j$. An overall good agreement between the simulations and the experimental estimations of the electron and ion heat conductivity was achieved (Fig. 1) except at the outer boundary where both the level and the variation tendency are in disagreement. Similar underpredictions of the heat conductivity by gyrokinetic simulations at the edge have been previously presented in Refs. [8,9].

The partial agreement of the full f modeling results achieved at the macro level was strengthened at the micro and intermediate turbulent scale level by comparisons to Doppler reflectometry [10] and Doppler enhanced scattering (ES) [10,11] microwave diagnostic measurements. Both diagnostics utilize backscattering of electromagnetic waves off low frequency small-scale density fluctuations in the vicinity of the cutoff for DR or the upper hybrid resonance (UHR) layer for ES to obtain information about small-scale fluctuation spectra and their perpendicular rotation. Characteristics of the two microwave systems including their spatial and wave number resolutions are presented in Table I. The frequency shift f_D between the

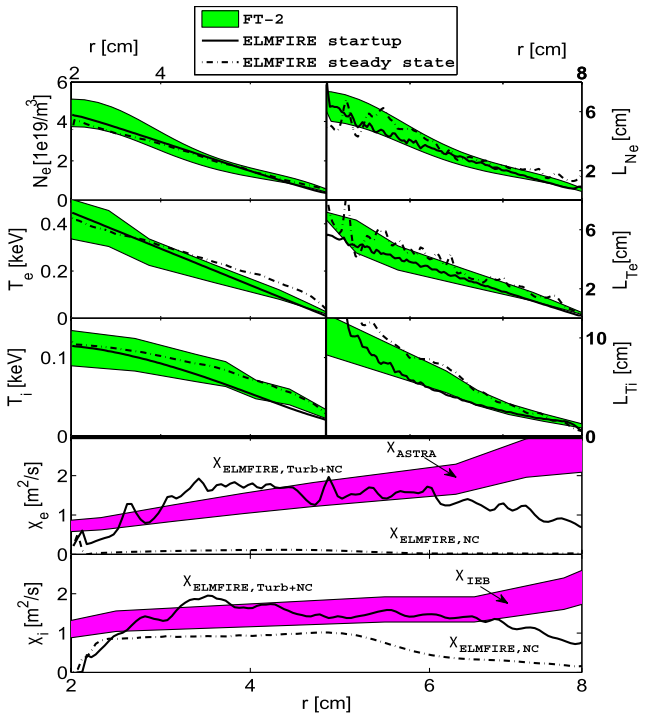

FIG. 1 (color online). The six top graphs: The experimental (shaded area) radial electron density (N_e), electron (T_e), and main ion (T_i) temperature profiles and the corresponding gradient scale lengths $L_s^{-1} = -\frac{d}{dr} \ln(s)$ compared to the ELMFIRE simulated flux surface averaged values at the startup (solid line) and at the end of the turbulent stage (dash-dotted line). The bottom two graphs: The radial flux surface and time averaged ELMFIRE predictions of the electron and main ion heat conductivity ($\chi_{e/i}$) in the turbulence (solid line) and neoclassical (dash-dotted line) stage compared to ASTRA ion energy balance predictions.

incident and backscattered wave can be related to the perpendicular velocity of the density fluctuations by $f_D = \mathbf{v}_\perp \cdot \mathbf{k}_\perp / 2\pi$ with $\mathbf{v}_\perp = \mathbf{v}_{E_r \times B} + \mathbf{v}_{\text{phase}}$, where $\mathbf{v}_{E_r \times B}$ is the plasma rotation velocity relative to the lab frame and $\mathbf{v}_{\text{phase}}$ the phase velocity of the density fluctuation in the plasma frame. Because of the fact that $B_\phi / B_\theta \gg 1$, the perpendicular motion of the density fluctuations is mainly in the poloidal direction. When the plasma is in an equilibrium state, no modulations in the phase velocity are expected, and changes in the radial electric field dynamics will lead to a direct change in $f_D(t)$.

TABLE I. Specifications of the microwave diagnostics.

Microwave diagnostic	Doppler reflectometry	Enhanced scattering
Propagation	Ordinary	Extraordinary
Incident freq.	26-36 GHz	54-66 GHz
k_θ range	3-5 cm^{-1}	15-30 cm^{-1}
Radial domain	0.8-0.9 r/a	0.65-0.87 r/a
Rad. resolution	$\approx$ 0.5 cm	$\approx$ 0.1 cm

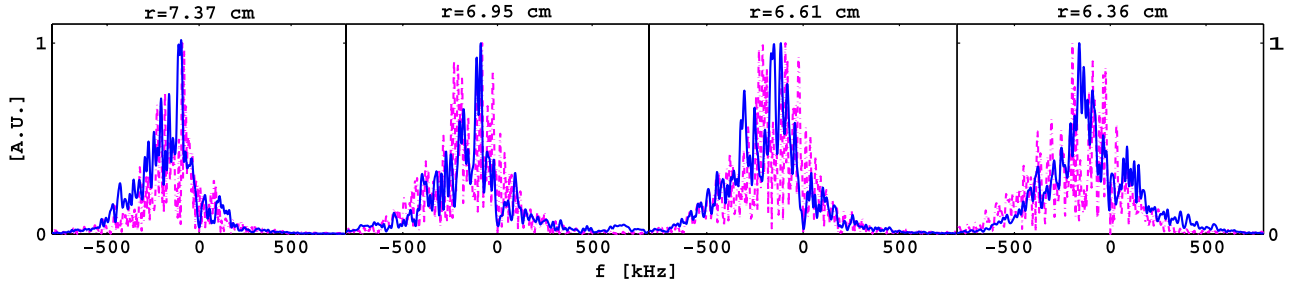

FIG. 2 (color online). DR spectra (solid line) compared to the corresponding synthetic Doppler spectra (dash-dotted line) from the ELMFIRE simulation including impurities at several radial positions.

Microscale turbulence frequency spectra measured by the DR diagnostic can be reconstructed through the relation $S(\omega) = \int_{-\infty}^{\infty} \int_0^{2\pi} \int_0^r dr d\theta dt r W(r,\theta)\delta n(r,\theta,t) e^{-i\omega t}$, where $W(r,\theta)$ is a complex weighting function, used to select the spatial and wave number range of the simulated density fluctuations $\delta n(r,\theta,t)$ [12]. Comparisons of the shape between the reconstructed and the experimental DR frequency spectra at several radii are shown in Fig. 2, where the statistical averages on the saturated nonlinear state are performed over 64 μs to obtain similar statistics. Not only the frequency shift but also the width and even the form of the experimental spectra are well reproduced by the synthetic diagnostic indicating comparable rotation and spreading of the selected turbulent density fluctuations. The fluctuation poloidal rotation velocity profile obtained from the mean frequency shift (the center of gravity of the frequency spectrum) of the experimental spectra is shown in Fig. 3(a) and is very close to that obtained from the synthetic spectra. However, it is slightly higher than the computed $v_{E_r \times B}$ plasma rotation profile averaged over the DR domain. This should be attributed to the fluctuation phase velocity, which appears to be smaller than the plasma rotation velocity. The poloidal velocity of drift-wave fluctuations responsible for probing wave backscattering in the UHR can equally be obtained from the mean value of the ES Doppler frequency shift and is also included in Fig. 3(a). These velocities appear to be close to those given by DR, indicating similar poloidal velocities for density fluctuations with different poloidal wave numbers. Here, the ELMFIRE code resolves for density fluctuations wider than the ion Larmor radius omitting the range of fluctuations responsible for probing wave backscattering in the UHR, and as such synthetic Doppler spectra cannot be produced for the ES diagnostic. ES diagnostics, however, have proven that the fluctuations of the electron temperature gradient scale and the scales between TEM and electron temperature gradient only play a minor role in the observed anomalous transport in FT-2 [13].

As usual in scattering experiments [14,15], the spectral width of the DR spectrum is larger (a factor of 2) than the value, prescribed by the wave number resolution technique. This difference is explained, in substantial part, by fast and strong variation of the radial electric field observed in modeling and shown in Fig. 4(a). These giant oscillations of the field at a frequency of approximately 30–50 kHz much smaller than the typical drift-wave frequency, but much larger than the inverse energy confinement time, can be attributed to the geodesic acoustic mode (GAM). This is supported by DR and ES measurements revealing similar oscillations in the poloidal velocity mesoscale dynamics. Applying the sliding Fourier transform (FT) procedure and the δ-phase method presented by Conway *et al.* [16] to the time signals obtained by the

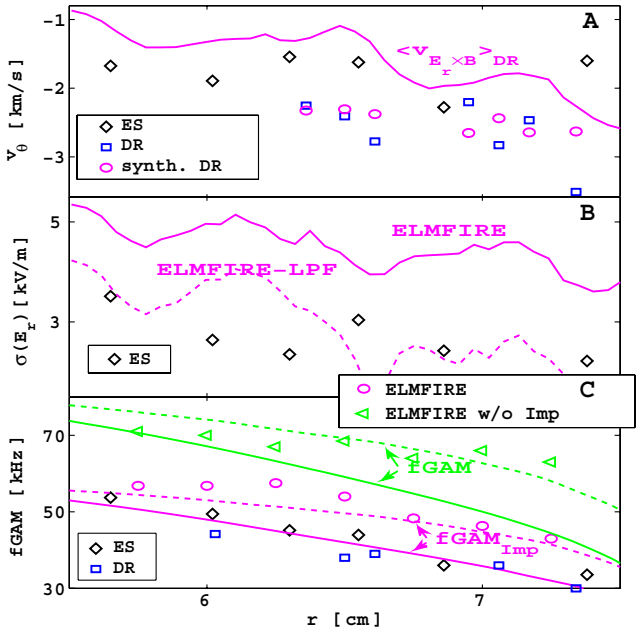

FIG. 3 (color online). (a) The poloidal velocity obtained from the ES (◇) and DR (□) measured frequency spectra and the synthetic DR spectra (o) compared to the $v_{E_r \times B}$ averaged over the DR domain. (b) The standard deviation of the simulated raw (solid line) and LP-filtered (dashed line) radial electric field fluctuations averaged over the ES domain compared to the ES measurements. (c) The dominant frequency of the ES (◇) and DR (□) measured radial electric field fluctuations compared to the ELMFIRE predictions with (o) and without (△) impurities included. The analytical predictions for the geodesic acoustic frequency with (pink) and without (green) impurities are presented for the startup (solid line) and steady state (dashed line) profiles.

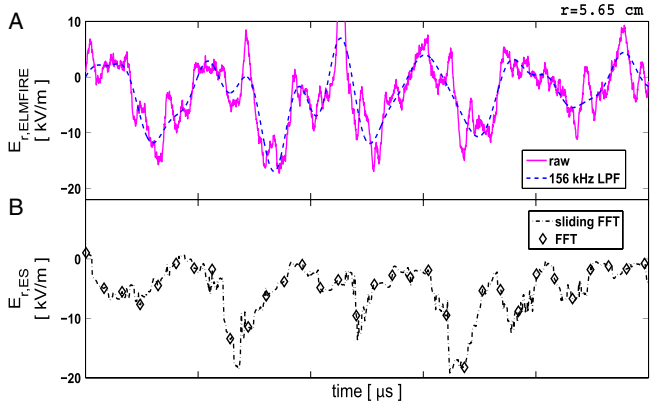

FIG. 4 (color online). (a) The simulated raw (solid line) and low-pass-filtered (dashed line) radial electric field time trace averaged over the ES domain centered at $r = 5.6$ cm for the turbulent saturated stage. (b) The radial electric field measured by ES at $r = 5.6$ cm analyzed with FT (◇) and sliding FT (dash-dotted line).

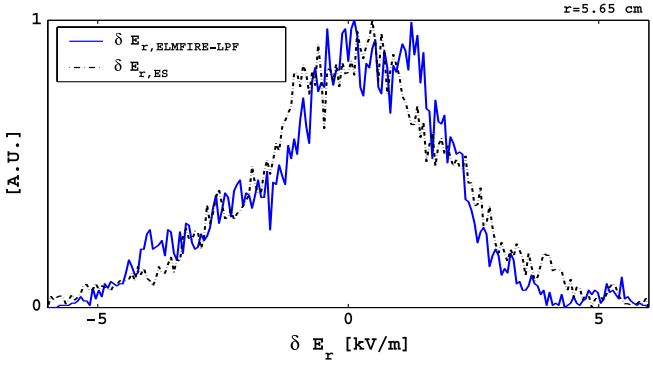

FIG. 5 (color online). The probability distribution function of the simulated LP-filtered (solid line) and sliding FT ES (dash-dotted line) measured radial electric field fluctuations at $r = 5.6$ cm.

backscattering techniques, one can generate $f_D(t)$ time sequences which by Fourier analysis gives the E_r spectrum and reveals the GAM-like spectral lines. In Fig. 3(c), the dominant E_r oscillation frequency dependence on the radius obtained by ELMFIRE simulations with and without impurities, the ES and DR measurements, are compared with the analytical GAM frequency presented by Guo *et al.* [17] in which the role of impurities is accounted for. For both the ELMFIRE simulations with and without impurities, the dominant frequency is fairly reproduced by Guo's analytical theory, whereas a good match of Guo's theory to the ES and DR results is found when the O^{+6} impurity component is accounted for.

The poloidal velocity mesoscale dynamics were studied in more detail by using the Doppler ES diagnostic possessing a much better spatial resolution and higher GAM spectra peak contrast (≈ 4) than the DR. The radial electric field time trace obtained with the Doppler ES technique is shown in Fig. 4(b). This $E_r(t)$ signal was constructed from scattering spectra with an FT window of 64 points and a sampling period of 50 ns, corresponding to a Nyquist frequency of $f_N = 156.25$ kHz. For one-on-one comparison, frequencies above the Nyquist frequency are removed from the simulated E_r time trace by a 156 kHz low pass filter, as demonstrated by the dotted line in Fig. 4(a). The probability distribution functions of radial electric field fluctuations $\delta E_r(t) = E_r(t) - \langle E_r(t)\rangle_t$, where $\langle E_r(t)\rangle_t$ is the time averaged mean, at the radial position presented in Fig. 4 are shown to be similar and well approximated by normal law, as shown in Fig. 5. The standard deviation of the δE_r probability distribution functions at various radial positions is presented in Fig. 3(b). At all radial positions, a good agreement is found between the simulated and experimental standard deviation when filtering is applied to the simulated data, whereas the nonfiltered simulated E_r fluctuations have significantly higher average amplitudes. It can be concluded that the simulations predict the correct GAM E_r amplitude, even though the GAM frequency is slightly overpredicted. This overprediction can be explained by the increased steady state temperature profiles caused by the underprediction of edge transport.

This work is supported by Grants No. 122435 and No. 134977 of the Academy of Finland, the EFDA Topical Group Activities, and the national Tekes work program. RFBR Grant No. 10-02-00631, the Russian Academy program Basic processes in high temperature magnetized plasmas, and the Russian government Grant No. 11.G34.31.0041 have financially contributed to this work. The HLST and the CSC IT Center for Science Ltd. CSC, DEISA, PRACE, and HPC-FF are acknowledged for the allocation of manpower and computational resources.

[1] P. H. Diamond, S.-I. Itoh, K. Itoh, and T. S Hahm, Plasma Phys. Controlled Fusion **47**, R35 (2005).
[2] P. W. Terry, Rev. Mod. Phys. **72**, 109 (2000).
[3] J. A. Heikkinen, S. J. Janhunen, T. P. Kiviniemi, and F. Ogando, J. Comput. Phys. **227**, 5582 (2008).
[4] T. Takizuka and H. Abe, J. Comput. Phys. **25**, 205 (1977).
[5] J. A. Heikkinen, T. Korpilo, S. J. Janhunen, T. P. Kiviniemi, S. Leerink, and F. Ogando, Comput. Phys. Commun. **183**, 1719 (2012).
[6] S. Leerink, Ph.D. thesis, Aalto University, 2012, http://lib.tkk.fi/Diss.
[7] G. V. Pereverzev and P. N. Yushmanov, Garching Report No. IPP 5/98, 2002.
[8] T. L. Rhodes *et al.*, Nucl. Fusion **51**, 063022 (2011).
[9] A. E. White *et al.*, Phys. Plasmas **15**, 056116 (2008).
[10] E. Z. Gusakov, A. D. Gurchenko, A. B. Altukhov, V. V. Bulanin, L. A. Esipov, M. Y. Kantor, D. V. Kouprienko, S. I. Lashkul, A. V. Petrov, and A. Y. Stepanov, Plasma Phys. Controlled Fusion **48**, B443 (2006).
[11] A. D. Gurchenko, E. Z. Gusakov, D. V. Kouprienko, S. Leerink, A. B. Altukhov, J. A. Heikkinen, S. I. Lashkul, L. A. Esipov, and A. Y. Stepanov, Plasma Phys. Controlled Fusion **52**, 035010 (2010).

[12] S. Leerink, V. V. Bulanin, E. Z. Gusakov, J. A. Heikkinen, S. J. Janhunen, T. P. Kiviniemi, T. Korpilo, M. Nora, and F. Ogando, Contrib. Plasma Phys. **50**, 242 (2010).

[13] A. D. Gurchenko and E. Z. Gusakov, Plasma Phys. Controlled Fusion **52**, 124035 (2010).

[14] P. Hennequin, R. Sabot, C. Honoré, G. T. Hoang, X. Garbet, A. Truc, C. Fenzi, and A. Quéméneur, Plasma Phys. Controlled Fusion **46**, B121 (2004).

[15] A. D. Gurchenko, E. Z. Gusakov, A. B. Altukhov, A. Y. Stepanov, L. A. Esipov, M. Y. Kantor, D. V. Kouprienko, V. V. Dyachenko, and S. I. Lashkul, Nucl. Fusion **47**, 245 (2007).

[16] G. D. Conway, B. Scott, J. Schirmer, M. Reich, A. Kendl, and (the ASDEX Upgrade Team), Plasma Phys. Controlled Fusion **47**, 1165 (2005).

[17] W. Guo, S. Wang, and J. Li, Phys. Plasmas **17**, 112510 (2010).